1 Production and Spectroscopy of Antihydrogen

C. Amsler, A. Giacomin, A. Glauser, O. Iannarelli, I. Johnson, H. Pruys, C. Regenfus, and J. Rochet

in collaboration with:
CERN, University of Aarhus, Brescia, Genoa, Pavia, RIKEN, Rio de Janeiro, Swansea, Tokyo

(ATHENA Collaboration)

The first observation of cold antihydrogen ($\bar{H}$) was reported in 2002 by the ATHENA collaboration [1]. This breakthrough has stimulated renewed interest in the field of low energy antimatter, and comparisons of the properties of antimatter with those of matter. For future laser spectroscopy experiments the temperature and quantum state of the $\bar{H}$ atom have to be controlled. In 2003 we therefore concentrated on the mechanism underlying the formation of $\bar{H}$, when low energy antiprotons are merged with a dense and cold positron plasma. We have also begun installing a laser system that allows specific $\bar{H}$ states to be addressed.

Antihydrogen is formed in a nested Penning trap by mixing 10^4 antiprotons with a positron plasma containing up to 10^8 particles at a temperature of 15 K. Low energy antiprotons from the CERN antiproton decelerator (AD) are moderated and captured in a Penning trap and are cooled to the ambient temperature of 15 K (1.3 meV) by a preloaded electron plasma. The capture efficiency is about 0.4 %, mainly determined by energy straggling in the absorber. Antihydrogen begins to form after the overlap of the antiprotons with the positrons, with initial production rates in excess of 300 Hz. The characteristics of the positron plasma such as the number of particles, the dimensions (typically 2 cm in length, 2 mm in width) and the density (10^8-10^9 cm^{-3}) can be obtained with a non-destructive method based on a measurement of the low-order axial electrostatic modes of the plasma [2]. The raw experimental data are the resonant frequencies of the first two modes (dipole and quadrupole), and the equivalent inductance of the plasma. The plasma diagnostic, coupled with radio-frequency heating, can be used to monitor and control changes in the plasma temperature. Antihydrogen formation at 15 K will be called "cold mixing" while positron-antiproton mixing with a positron plasma heated to $\approx$3000 K will be referred to as "hot mixing".

The neutral $\bar{H}$'s are not confined by the electric and magnetic fields and therefore migrate to the trap walls where they annihilate. These events are monitored by the $\bar{H}$ detector built by the University of Zurich [3]. The detector consists of two layers of double-sided silicon strip detectors to register the charged annihilation pions and to reconstruct the annihilation vertex. Antihydrogen is detected by requiring the spatial and temporal coincidence of the vertex with two back-to-back 511 keV γ's produced by the annihilation of the positron. The γ's are detected by a high granularity electromagnetic detector comprising 192 CsI crystals with avalanche photodiode readout. A comprehensive description of the ATHENA apparatus can be found in ref. [4].

1.1 Antihydrogen production efficiency

The observation of cold $\bar{H}$ was based on a complete reconstruction of its annihilation, in which both antiprotons and positrons were detected via their annihilation products. We reported 131 ± 22 "golden events" [1]. However, the detection efficiency was low ($\simeq$ 0.2%), mainly due to the 20% detection efficiency for each of the two 511 keV photons, and stringent software cuts. In a further analysis [5] we show that the trigger rate during cold mixing is due to two sources: $\bar{H}$ production itself

comprises over 85% of the triggers at the beginning of mixing, and declines with a time constant of several seconds. Antiproton annihilation on positive ions or on rest gas (with a slowly decreasing rate) comprises the remainder of the triggers. During a complete cold mixing cycle $\bar{H}$ production accounts for (65 $\pm$ 5)% of the total integrated trigger rate. Thus in 2002 almost 500,000 $\bar{H}$ atoms were produced.

In Fig. 1.1 (left) we show the photon energy spectrum for cold mixing and for antiprotons only, normalized to the same number of annihilation vertices. No peak is observed at 511 keV for the annihilation of antiprotons only. This is good news since we feared earlier that the background from positron annihilation from high energy showers in the surrounding coils would be much more severe. The difference plot (Fig. 1.1, right) shows the 511 keV line from positron (antihydrogen) annihilation, together with a pure positron (no $\bar{p}$) annihilation spectrum. Peak position and resolution agree.

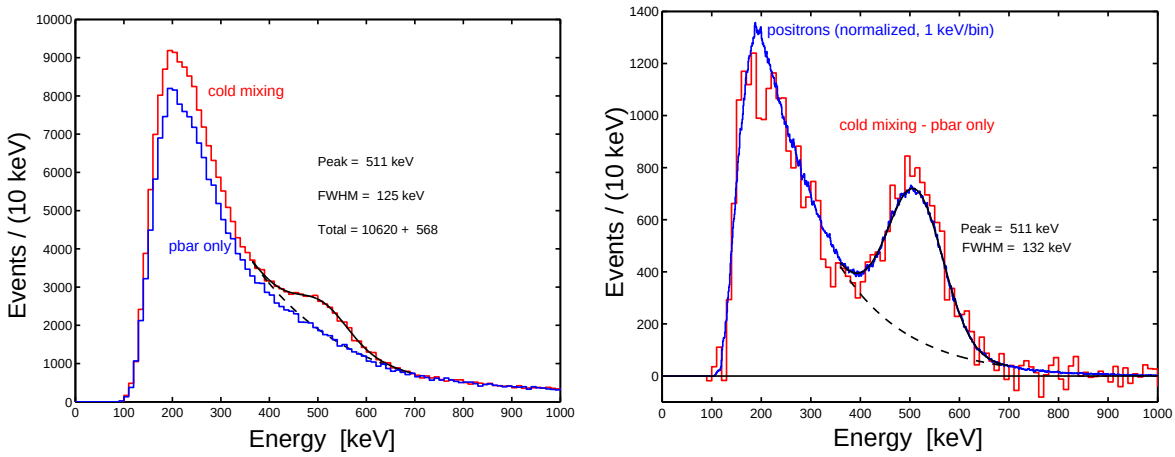

Figure 1.1: *Left: photon spectrum (sum of the 162 best crystals) for cold mixing and antiprotons only. Right: difference plot and annihilation spectrum from a pure positron plasma superimposed.*

1.1.1 Orthopositronium production

The detection of antihydrogen relies on the reconstruction of two back-to-back 511 keV photons. However, orthopositronium could be produced when positrons annihilate on the trap walls. The contribution from orthopositronium (which decays into 3γ) is unknown since it depends on a possible frozen gas layer on the trap electrode surface at cryogenic temperatures. A large production rate could lead to an underestimate of our antihydrogen formation rate.

A dedicated measurement with positrons only was therefore performed to determine the relative rates of the 2γ and 3γ decay modes of e^+e^- annihilations for antihydrogen atoms interacting with the electrode surfaces [5]. The electrostatic well holding the positrons was modified so that the radial outward transport of positrons onto the trap electrodes was strongly enhanced. The photons produced in positron annihilations at the surface of the electrodes were detected in the photon detector. The trigger condition required the detection of at least two photons with an energy greater than 150 keV each. For events containing two or three photons, the total energy E_{tot} and the total momentum P_{tot} were determined. Figure 1.2a shows the clear signal from 2γ events at $E_{tot} = 2m_ec^2$ and $P_{tot} < 200$ keV/c. The accumulation of events at $P_{tot} = E_{tot}$ stems from 2γ events for which one γ escaped detection, while the other underwent Compton scattering in the first crystal before being absorbed by the second adjacent crystal. This process also accounts for most detected 3γ events, stemming from

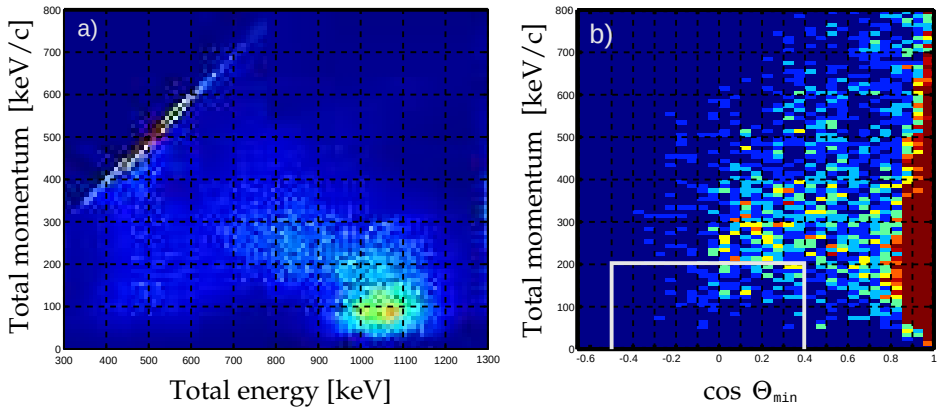

Figure 1.2: *a) P_{tot} vs. E_{tot} for 2γ-events; b) P_{tot} vs. cosine of the minimum 2γ-opening angle for 3γ events. The box shows the expected region for orthopositronium annihilation.*

2γ events, for which one γ is Compton scattered in a first and detected in a second crystal. Figure 1.2b shows a distribution for 3γ events satisfying the condition $|E_{tot} - 2m_e c^2| < 200$ keV. The total momentum of the 3γ is plotted versus the smallest of the three angles between any 2γ. Compton scattered photons accumulate at small angles. The box indicates the expected orthopositronium signal region. The detection probabilities for the two decay modes were evaluated by Monte Carlo simulation. From the observed number of events we could conclude that 2γ events account for at least 95% of all e^+e^- annihilations.

1.1.2 Optimization of $\bar{H}$ Rate

Combining hot and cold mixing data we have produced so far in excess of 2 million $\bar{H}$ atoms. However, this corresponds only to about 17% of the antiprotons injected into the trap. Possibilities to increase this formation rate were studied in 2003. For example, positron plasma compression can be achieved using the so-called "rotating wall" method in which the plasma is spun by applying a rotating electric field of several hundred kHz to a segmented trap electrode. The segmented Faraday cup detector in the positron accumulator was replaced with a phosphor screen and an auxiliary low-noise CCD camera. This enables a more accurate measurement of the position and size of the positron plasma (Fig. 1.3) before it is transferred to the ATHENA mixing trap located inside the main 3T magnet. We achieved plasma densities of up to 10^{10} e^+ cm^{-3}, which is the highest density positron plasma achieved worldwide to date.

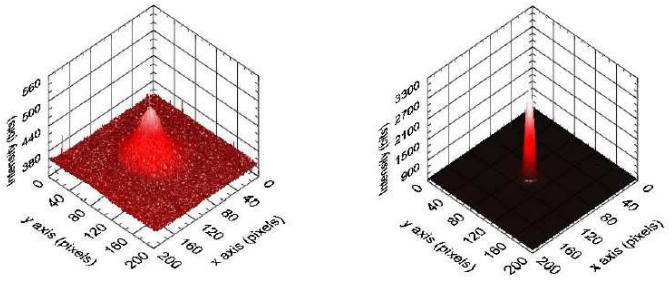

Figure 1.3: *CCD images of the position and size of the positron plasma dumped on the phosphor screen in the positron accumulator without (left) and with (right) rotating wall compression.*

Attempts were also made to increase the number of positrons available for $\bar{H}$ formation by stacking successive shots of positrons from the positron accumulator in the mixing trap. Figure 1.4 shows the number of stacked positrons in the main magnet versus the number of transfers. In this way we were

able to reach positron plasmas containing 1.2 $\times$ 10^9 positrons, again the highest number of stored positrons achieved anywhere to date.

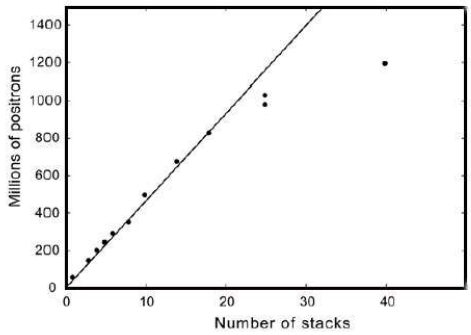

Figure 1.4: *Stacking successive shots of positrons from the positron accumulator. The line is a fit to the data up to 20 stacks and shows the linear behaviour. The fit shows that 50 million positrons per stack were captured.*

Modifications to the ATHENA trap are being carried out to implement the so-called "side band excitation" of the radial $\bar{p}$ motion to reduce the $\bar{p}$ plasma size and increase the overlap with the e^+ cloud: due to the degrader foil, captured antiprotons have large initial axial, magnetron, and modified-cyclotron amplitudes. While the axial and cyclotron motions are quickly damped through collisions with electrons, the large magnetron radii of the confined antiprotons are retained throughout the entire stacking, transfer, and measurement cycle. This leads to both reduced transfer efficiency and reduced $\bar{H}$ production due to poor radial overlap with the positron plasma. The two independent radial motions carried out by charged particles, the magnetron motion and the modified cyclotron motion, can be resonantly excited by azimuthal radio-frequency electric fields. Quadrupolar excitation at the sum frequency of the two modes (the true cyclotron frequency, 45 MHz in ATHENA) leads to a coupling and energy exchange between them. In the absence of a cooling mechanism, this can be used to transform low-frequency, low-energy magnetron motion into high-frequency, high-energy cyclotron motion. In the presence of a cooling mechanism the modified cyclotron motion would be quickly damped and the total radial motion centered. No significant improvement in the $\bar{H}$ production rate was achieved so far. This issue will be pursued in 2004.

1.2 Dynamics of antihydrogen formation

We have measured the antiproton energies during cooling and while $\bar{H}$ is efficiently formed [6]. Figure 1.5 shows the measured antiproton energy spectra at various times during the mixing cycle and Fig. 1.6 the W-shaped nested penning trap potential with the positrons in the middle. The antiprotons were ejected from the entrance well and their intensity measured as a function of electric potential. The antiproton potential energy is divided into three regions (labeled I-III in Fig. 1.5. Region I corresponds to $\bar{p}$ energies larger than positron energies, region II to $\bar{p}$'s within the positron space charge, whilst in the lowest energy region III antiprotons no longer have sufficient kinetic energy to penetrate the positron cloud.
The antiprotons ejected from the left well under cold mixing conditions begin to cool rapidly and after about

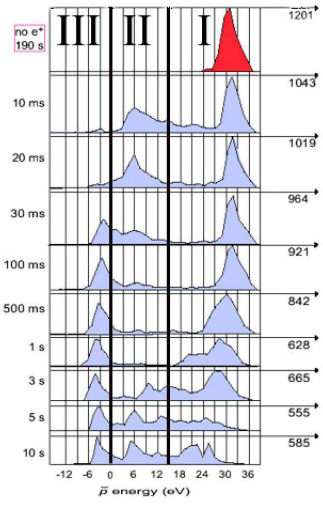

Figure 1.5: *Antiproton energy spectra for different interaction times, shown on the left. The maximum number of events per channel in each distribution is indicated on the right. The vertical thick lines divide the three energy regions (see text)*

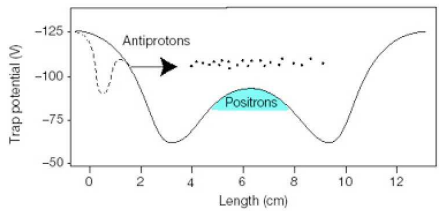

Figure 1.6: *Nested Penning trap potential*

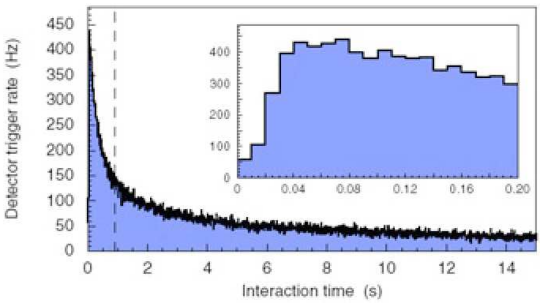

Figure 1.7: *Trigger rate vs. time for cold mixing. The inset shows an expansion of time between 0 and 0.2 seconds illustrating the onset of $\bar{H}$ production at about 20 ms.*

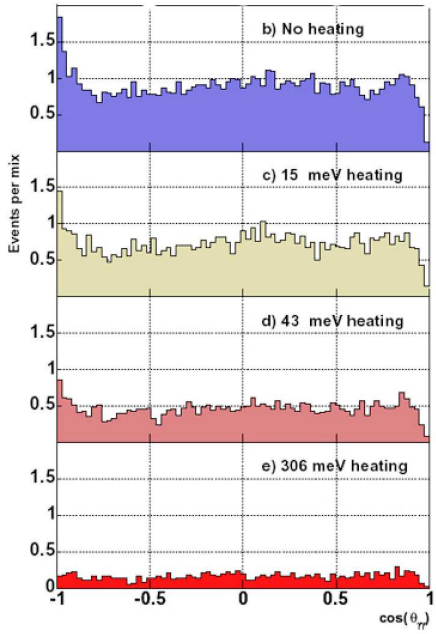

Figure 1.8: *Cosine of the opening angle distribution for different positron plasma temperatures $\sim$ 15 K, 190 K, 515 K and 3500 K (top to bottom, normalized to the mixing of 10'000 $\bar{p}$ with 7$\times$ 10^7 e^+). The peak at -1 is due to e^+e^- annihilation of $\bar{H}$ atoms hitting the electrodes.*

20 ms a significant fraction ($\simeq$ 40%) reach energies close to the bottom of the positron well. It is here that they are moving slowest as they traverse the positron cloud, and under these conditions one might expect $\bar{H}$ to form. This is borne out by the data shown in Fig. 1.7 where the $\bar{H}$ detector trigger rate shows a dramatic increase after 20 ms. On longer time scales, though $\bar{H}$ is still copiously formed, there are many antiprotons that retain kinetic energies close to those on injection. This indicates only weak coupling to the positron plasma, possibly due to poor radial overlap. There is also a slow transfer of antiprotons into region III, since antiprotons are present in both the left and right wells at longer times. The precise manner in which the antiprotons cool below the lowest positron energy is not yet clear, but may involve field ionisation of weakly bound $\bar{H}$. A measurement without positrons is included in Fig. 1.5 and, as expected, no antiproton cooling is apparent.

We have also measured the temperature dependence of $\bar{H}$ formation [7]. The two processes that lead to $\bar{H}$, radiative combination (in which a photon removes the binding energy) and three-body combination (in which a second positron removes the excess energy), lead to different n-state distributions. The former populates mainly the low n states and the latter mainly the high n states. The $\bar{H}$ production rate has also a different dependence on temperature, $T^{-1/2}$ for the former and $T^{-9/2}$ for the latter.

As explained above, the positron plasma temperature could be changed in a controlled way by radio-frequency excitation. The minimum measurable temperature increase was about 15 meV ($\sim$ 175 K). The electrode temperature of 15 K was the lower limit for the unheated plasma, and this was adopted as the unperturbed temperature. Mixing was carried out at different positron plasma temperatures including the cold mixing data (15 K) and three other high statistics hot mixing samples at 190 K, 515 K and 3500 K. The measurements were analyzed in a variety of ways by measuring (a) the 2γ opening angle excess enhancement, (b) the number of triggers for all samples and (c) the peak trigger rates for the high statistics samples. The 2γ opening angle distribution is shown in Fig. 1.8.

One observes from the enhancement at low $\cos\Theta_{\gamma\gamma}$ that $\bar{H}$ production decreases with temperature, but is still produced at room temperature. This favours radiative over three-body combination.
The temperature dependence of $\bar{H}$ is shown for the three methods in Fig. 1.9. One observes a clear decrease of the $\bar{H}$ production with positron plasma temperature. However, a simple power law does not fit the data. The three-body temperature dependence ($T^{-9/2}$) is not consistent with data. Again this favours radiative over three-body recombination. However, the radiative rate prediction is not obviously compatible with our data, being an order of magnitude lower. More work is necessary to definitively clarify the underlying mechanism.
We also measured the spatial distribution of the emerging $\bar{H}$ atoms which can also provide insights into dynamics of the formation process and the distribution of initial atomic states. Figure 1.10 shows the measured distribution compared to a set of model distributions. The model that best matches the measurements is a slightly anisotropic distribution with a small radial excess. The near-isotropic nature of the distribution suggests that $\bar{H}$ is mostly formed when the antiprotons are diffusing randomly in the positron plasma. Calculations suggest that weakly bound states (populated mostly by the three-body mechanism) would emerge along the lines of the magnetic field. Therefore, the observed isotropic emergence suggests that three-body combination may not be the dominant $\bar{H}$ formation mechanism in ATHENA, in accord with the temperature measurements discussed above.

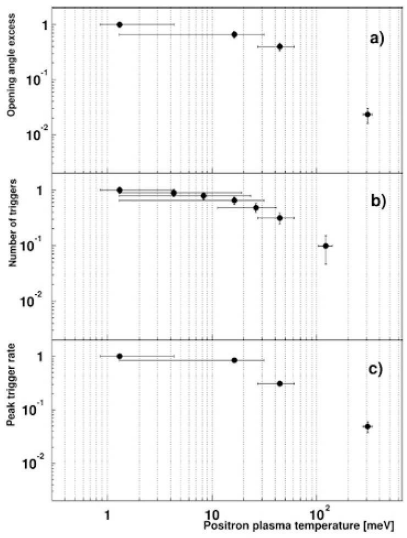

Figure 1.9: *Temperature dependence of $\bar{H}$ production (a) for the opening angle excess, (b) the number of triggers, and (c) the peak trigger rates. Data are normalised to the 15 K sample.*

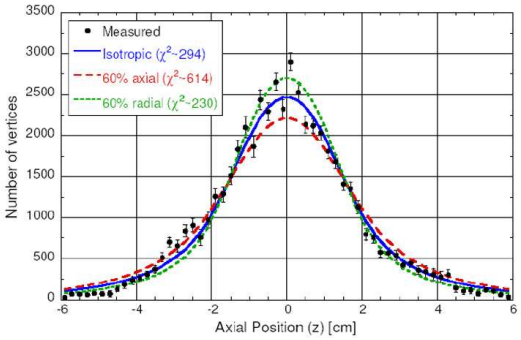

Figure 1.10: *Comparison between isotropic, axially and radially enhanced axial vertex distributions of $\bar{H}$ annihilations. A typical plasma length of 32 mm was used. The data are almost compatible with isotropic emission (blue curve).*

1.3 Measurements and improvements on detector performances

Improvements to the detector readout were made to enhance the sensitivity and extend the capabilities of the ATHENA apparatus. The 32 Si μstrip modules of the detector are now read out in a zero suppressed mode so that the detector can be read out at a much higher rate of 200 Hz. One consequence is a substantial increase in baseline fluctuations in the raw crystal data. At readout rates near 200 Hz electronic baselines of the crystals can fluctuate by more than 5 times the average noise. The readout chips are the cause of these fluctuations, since each row of 12 crystals is read out by one readout chip and baselines of crystals within each row move together. Figure 1.11 illustrates the row-by-row correlation of the baseline fluctuations. New row-by-row baselines for each event are calculated by

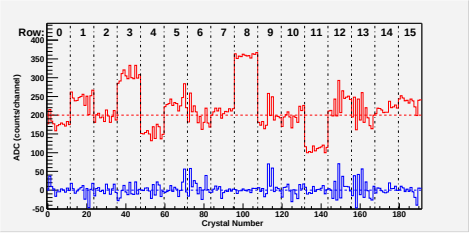

Figure 1.11: *ADC versus crystal channel distributions for a typical readout rate near 200 Hz. Upper distribution: before common-mode-noise correction (artificially offset from 0 by 200 ADC counts). Note the common offsets for rows of 12 crystals connected to the same amplifier chip. Lower distribution: after a row-by-row common-mode-noise correction.*

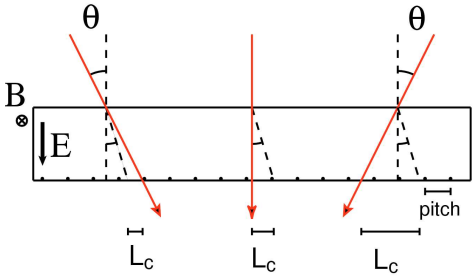

Figure 1.12: *The Lorentz angle λ leads to different cluster lengths L_c that depend on the incident angle θ.*

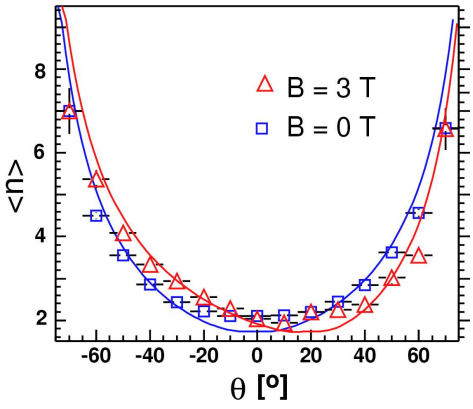

Figure 1.13: *Cluster size distribution for tracks in the plane perpendicular to the detector axis as a function of θ.*

averaging the ADC values of the groups of 12 crystals (ignoring of course crystals with signals). The new row-by-row baselines are subtracted from the data to obtain ADC distributions that oscillate around zero, see Fig. 1.11.

1.3.1 Measurement of the Lorentz angle

In the presence of the 3 T field the charge carriers (the holes in our detector) do not migrate radially along the electric field but are deflected by the Lorentz angle. Hence the cluster size of the collected charge is modified and its centroid displaced on the readout side. Under the drift along the Lorentz angle λ, the cluster lengths L_c is shortened for tracks that traverse the silicon at angles in the direction of the Lorentz deflection, and increased for tracks that cross in the opposite direction (Fig. 1.12).
Our sensors are oriented around two cylinders. The propagation direction of the holes is inward for the inner layer and outward in the outer layer. This results in opposite Lorentz angle displacements that can substantially modify the helix parameterization of the tracks and deteriorate the determination of the annihilation vertex.
We therefore measured the Lorentz deflection angle λ at 130 K. Measurements were made with cosmic rays with field off and on. Figure 1.13 shows for example the average cluster size (number of adjacent hit strips) for tracks in the plane perpendicular to the detector axis ($\phi \simeq 0$) and traversing the silicon layer under the angle θ. The symmetry about θ = 0 in the field off data indicates that charge is propagating along the electric field perpendicular to the plane of the silicon, as expected, while the asymmetry in the distribution of the 3 T data clearly indicates that the holes propagate along a non-zero Lorentz angle.
Since the cluster size also depends on the total charge deposited and hence on the track inclination ϕ along the detector axis, the data were subdivided in ϕ intervals and fits were performed for each bin to determine λ. The strip pitch (139.5 μm) and detector thickness (380 μm) were fixed to their known values, while the charge detection threshold was left as a free parameter. The results shown in Fig. 1.14 do not depend on ϕ, as expected. We obtain a Lorentz angle λ = (18.8 $\pm$ 0.5) $^\circ$ for holes at 130 K and 3 T, while for the field off data λ was consistent with zero.
In order to correct for the displacement caused by the drift along the Lorentz angle, all cluster positions were then shifted by -64.5 μm in the $\vec{E} \times \vec{B}$ direction. This led

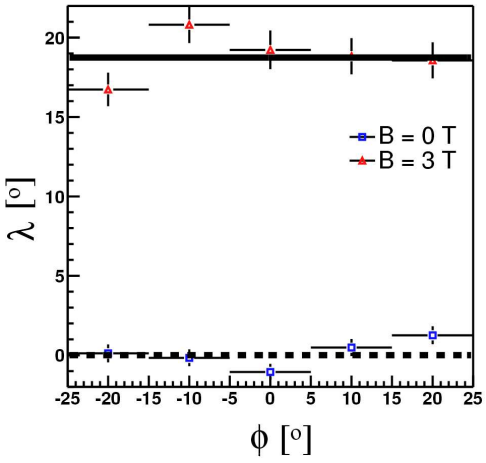

Figure 1.14: *Distribution of the Lorentz angle λ vs. ϕ (track angle along the detector axis) for field on and off.*

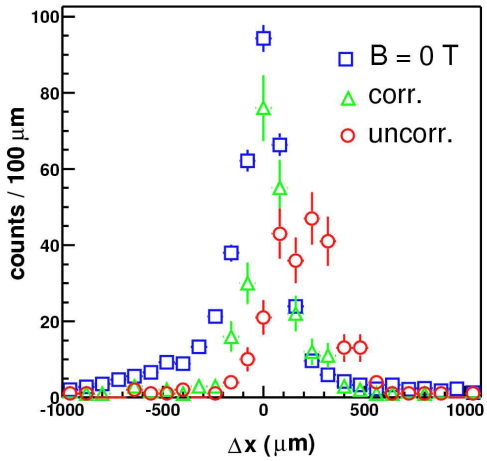

Figure 1.15: *Shift in the reconstructed position of traversing cosmic rays for field on (red) and off (blue). The shifts after correction are shown in green.*

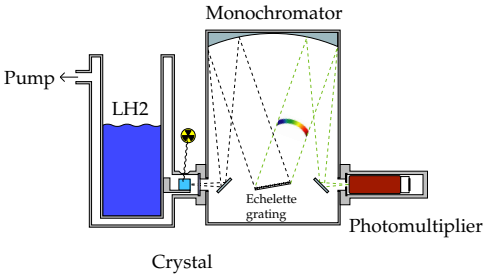

Figure 1.16: *Optical spectrometer to measure the light yield of scintillator crystals as a function of temperature and wavelength.*

to a significant improvement in the residuals for traversing cosmic rays which are now in good agreement with the unaffected field off distributions (Fig. 1.15).

1.3.2 R & D on CsI crystals

Pure CsI was chosen in ATHENA because of the excellent light yield at low temperature [8]. Initially, the crystals were coupled to pn photodiodes, but their performances deteriorated with time, due to corrosion from the iodine of CsI. We therefore replaced them with avalanche photodiodes (APD) which have gains and hence much better signal-over-noise ratios. A systematic study of the response of SINTEF and avalanche photodiodes as a function of temperature and wavelength was performed with an optical spectrometer based on an Echelette grating [9].
In 2003 we modified this facility to measure the light emission spectrum of scintillation crystals as a function of wavelength and temperature. Figure 1.16 shows the apparatus. A 50 MBq ^{90}Sr electron source irradiates a CsI crystal kept at liquid nitrogen temperature. The monochromator is equipped with a spherical mirror to image the entrance slit with parallel light to the exit slit after the grating. The crystal is located on a cold finger (see Fig. 1.17) at the focus of the monochromator.

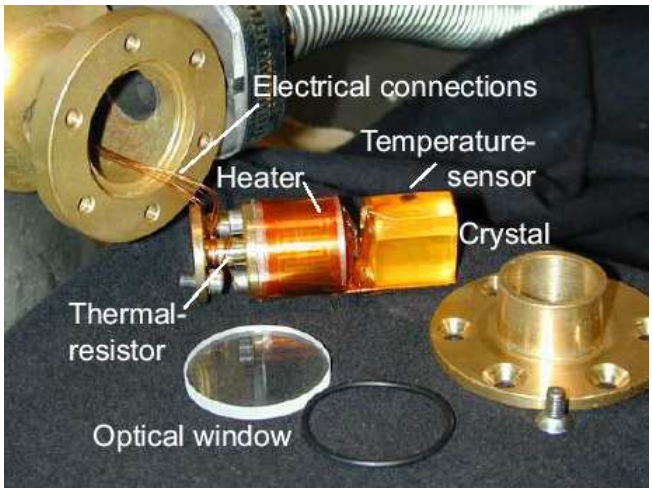

Figure 1.17: *Cold finger and vacuum chamber. The crystal is attached to the copper support with a capton tape. The brass piece on the right is used to press the optical window to the gasket ring and fits into the entrance slit of the monochromator.*

To reach liquid nitrogen temperatures a good vacuum is needed to prevent heat flow through the short

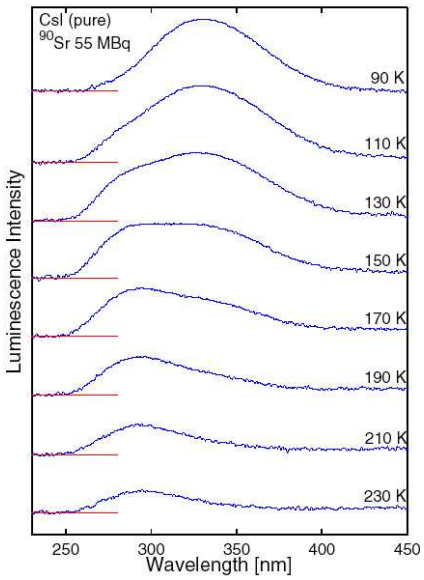

Figure 1.18: *Emission spectra from pure CsI crystal at different temperatures. The logarithmic vertical scale is in arbitrary units.*

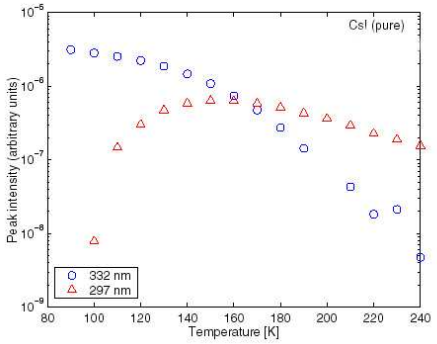

Figure 1.19: *Intensity of the emission lines at 332 nm and 297 nm as a function of temperature.*

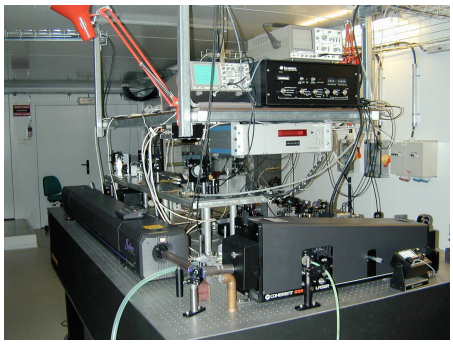

Figure 1.20: *Photograph of the krypton and dye lasers on the optical bench.*

distance (1 mm) between the cold finger and the wall of the chamber at room temperature. A turbo vacuum pump is used and a vacuum below $2\times\ 10^{-6}$ mbar can be achieved. The Echelette grating is slowly rotated while the light intensity is measured with a photomultiplier. The current of the photomultiplier is integrated and measured with an electrometer.

Data were taken in temperature steps of 10 K between 90 and 230 K for wavelengths between 240 and 450 nm. The emission spectrum contains two lines (Fig. 1.18) which were fitted with gaussians and a smooth background. The relative intensities of the fitted emission lines at 297 and 332 nm are shown in Fig. 1.19 as a function of temperature. The presence of two emission lines in pure cold CsI was already known before [10]. However, our measured intensity distributions are much more precise.

1.4 R&D for laser spectroscopy

In 2003 our group group was involved in the preparation of the spectroscopy phase, namely the construction of a laser system to generate 243 nm light for 1s-2s two-photon spectroscopy in antihydrogen [11]. We used the well known non-linear technique to generate 243 nm light from a laser source of longer wavelength. The laser system consists of a Kr^+ ion laser that emits 4 W in the range 406 nm to 415 nm. The (up to 6 W) Kr^+ ion laser pumps a dye laser which emits in the range 460 nm to 516 nm. The dye laser is tuned to a wavelength of 486 nm which is twice the wavelength of the two-photon 1s-2s transition in (anti)hydrogen. Most of the equipment was provided by the University of Aarhus. A photograph of the two lasers is shown in Fig. 1.20.

The light from the dye laser is sent into an external frequency doubling cavity containing a nonlinear crystal. The second harmonic generation power in the crystal is maximum when the refractive indices n for the fundamental and the second harmonics are equal. Since the refractive index depends on frequency, a birefringent crystal with a suitably oriented optical axis is used, in which the ordinary ray is chosen for the fundamental frequency and the extraordinary ray for the second harmonic, i.e. $n_o(\omega) = n_e(2\omega)$. Losses are reduced by using a crystal cut such that the light with fundamental frequency traversing the crystal penetrates the crystal under the Brewster angle. Under this angle the polarisation parallel to the plane formed by the incident beam and the normal to the crystal surface is not reflected but transmitted into the crystal. The wavelength can be measured accurately with a Michelson interferometer with moving mirrors, calibrated on a He-Ne laser.

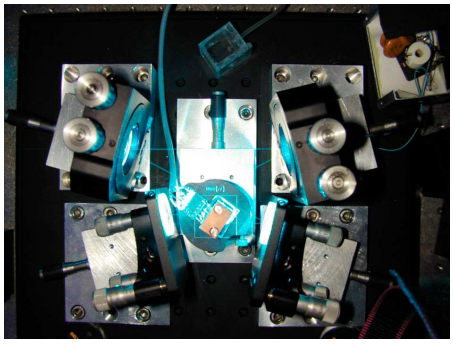

Figure 1.21: *Photograph of the lasing cavity. The crystal is mounted inside the temperature stabilized copper block in the center of the picture.*

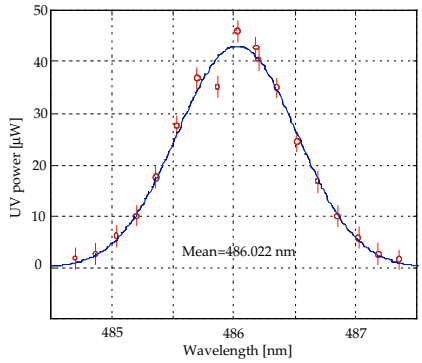

Figure 1.22: *Tuning the dye laser to 486 nm (input power 45 mW).*

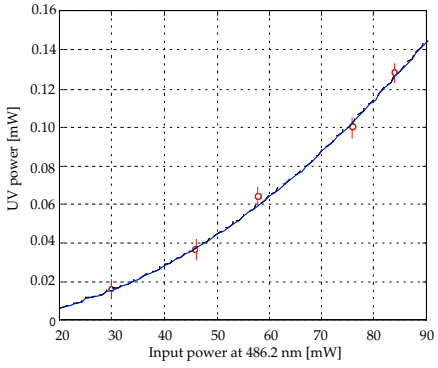

Figure 1.23: *The 243 nm cavity output power as a function of 486 nm input power. The curve shows the expected quadratic dependence.*

The cavity - Fig. 1.21 - consists of a Brewster cut rhomb shaped beta barium borate (BBO) crystal of dimensions $5 \times 5 \times 8$ mm^3. The light from the dye laser enters from the right. The convex mirrors have a reflection coefficient of 100 % for the first harmonic and a transmission coefficient of 95 % for the second harmonic. One of the mirrors is mounted on piezoelectric crystal to vary the optical path-length in the cavity. The beam is sent to a photodiode for cavity locking. The cavity was developed by the Zurich team and the mechanical stability of the piezo was investigated in details [11]. The support structure and temperature stabilized crystal holder (to better than 0.1°) were built in the mechanical workshop of our institute.

Figure 1.22 shows the tuning of 486 nm light from the dye laser. Unfortunately the specified output power of the dye laser (360 mW of power at 486 nm for 3 W input power) could not yet be achieved. The power output is an order of magnitude smaller than expected. However, second harmonic generation of 243 nm UV light was achieved in the BBO cavity. Figure 1.23 shows the output power at 243 nm as a function of input power at 486 nm. The measurement agree with the prediction that the second harmonic power increases with the square of the input power (curve).

[1] M. Amoretti *et al.*, Nature **419** (2002) 456.
[2] M. Amoretti *et al.*, Phys.Rev.Lett.**91** (2003) 055001.
[3] C. Regenfus, Nucl.Instr.Meth.**A 501** (2003) 65.
[4] M. Amoretti *et al.*, Nucl.Instr.Meth.**A 518** (2004) 679.
[5] M. Amoretti *et al.*, Phys.Lett.**B 578** (2004) 23.
[6] M. Amoretti *et al.*, submitted to Phys.Lett.**B**.
[7] M. Amoretti *et al.*, Phys.Lett.**B 583** (2004) 59.
[8] C. Amsler *et al.*, Nucl.Instr.Meth.**A 480** (2002) 494.
[9] A. Glauser, Diplomarbeit, Universität Zürich, 2003.
[10] H. Nishimura *et al.*, Phys.Rev.**B 51** (1995) 2167.
[11] O. Iannarelli, Diplomarbeit, Universität Zürich, 2004.